MATERIALS SCIENCE

Structured silicon for revealing transient and integrated signal transductions in microbial systems

Xiang Gao[1]*†, Yuanwen Jiang[1,2†], Yiliang Lin[1†], Kyoung-Ho Kim[3,4†], Yin Fang[1], Jaeseok Yi[1], Lingyuan Meng[5], Hoo-Cheol Lee[3], Zhiyue Lu[6], Owen Leddy[1], Rui Zhang[5], Qing Tu[7], Wei Feng[5], Vishnu Nair[2], Philip J. Griffin[5], Fengyuan Shi[8], Gajendra S. Shekhawat[7], Aaron R. Dinner[1,2,9], Hong-Gyu Park[3]*, Bozhi Tian[1,2,9]*

Bacterial response to transient physical stress is critical to their homeostasis and survival in the dynamic natural environment. Because of the lack of biophysical tools capable of delivering precise and localized physical perturbations to a bacterial community, the underlying mechanism of microbial signal transduction has remained unexplored. Here, we developed multiscale and structured silicon (Si) materials as nongenetic optical transducers capable of modulating the activities of both single bacterial cells and biofilms at high spatiotemporal resolution. Upon optical stimulation, we capture a previously unidentified form of rapid, photothermal gradient–dependent, intercellular calcium signaling within the biofilm. We also found an unexpected coupling between calcium dynamics and biofilm mechanics, which could be of importance for biofilm resistance. Our results suggest that functional integration of Si materials and bacteria, and associated control of signal transduction, may lead to hybrid living matter toward future synthetic biology and adaptable materials.

INTRODUCTION

Bacterial ensembles can behave like multicellular and adaptable organisms through intercellular communication and cooperation (*1*–*3*). For example, quorum sensing (Fig. 1A), which is switched on at high cell densities, enables coordinated behaviors (*1*), such as massive virulence factor secretion and immune suppression of the host. Recently, electrochemical signaling mediated by potassium ion channels (Fig. 1A) was found to be crucial for long-range communication within biofilms (*2*, *4*), which makes the colony more resilient to nutrient depletion and other environmental changes. While these reported modes of intercellular communications take minutes or even hours to become effective (table S1) (*2*, *3*, *5*), fast intercellular signaling, a well-characterized phenomenon in mammalian cells (*6*), has seldom been explored in microbial systems. Our knowledge of how bacteria respond or adapt to transient physical insults [e.g., thermal (*7*) and mechanical shocks (*8*)] is also limited, although such cellular responses are likely crucial to their survival in the highly dynamic natural environment (*9*).

Existing interrogation tools lack the desired spatiotemporal precision to study fast microbial signal transduction in response to transient perturbations. The stimuli are typically delivered by injection and subsequent diffusion, taking seconds to equilibrate. Therefore, only slow or global changes in metabolic activities (*10*), gene expression levels (*11*), medium compositions (*12*), and thermal (*13*) or mechanical environments (*14*) can be induced. Optical modulation techniques (*15*) using various nongenetic transducers hold great promise for introducing transient (*16*) (down to millisecond level), localized (*17*) (with an arbitrarily aimed diffraction-limited spot), multiplexed (photothermal, photocapacitive, photofaradaic, and photoacoustic) (*18*), and controllable (in duration and intensity) perturbations (*17*) to the microbial community. Among existing material candidates for optical modulation, silicon (Si) stands out as unique (*19*, *20*), given its known biocompatibility (*21*), well-characterized photoresponses (*22*), and mature manufacturing technologies (*23*). Optically controlled Si materials are widely used in a variety of mammalian systems for either biophysical probing (*24*) or biomedical applications (*22*, *25*, *26*). Here, we extend the utility of Si to the study of transient intercellular signaling in bacteria (Fig. 1B). We have designed a variety of structured Si materials, which fit different bacterial systems and allow delivery of optically induced transient and local stresses.

RESULTS

In nature, bacteria exist in two distinct forms: isolated planktonic cells (Fig. 1C), several micrometers in size, that can move freely, and biofilms (Fig. 1D), several centimeters in size, where a concerted community of cells is embedded in a self-produced matrix of extracellular polymeric substances (*27*). To target bacteria with such vastly different dimensions, one basic design principle is to use a series of Si structures spanning multiple length scales for size-matched biointerfaces (*22*).

As interfaces with planktonic bacteria, we considered Si nanowire because the material's one-dimensional (1D) geometry and submicrometer-scale dimension are close to those of the rod-shaped cells (Fig. 1C and table S2), allowing the potential for single-cell manipulation. We selected mesostructured nanowires, rather than single crystalline ones, to enhance light absorption as well as Si-bacteria interaction (*28*). Using a defect-selective etching (*29*) of the grain boundaries in coaxial nanocrystalline Si nanowires, we synthesized hierarchical, flake-like mesostructures with a high degree of surface

[1]James Franck Institute, The University of Chicago, Chicago, IL 60637, USA. [2]Department of Chemistry, The University of Chicago, Chicago, IL 60637, USA. [3]Department of Physics, Korea University, Seoul 02841, Republic of Korea. [4]Department of Physics, Chungbuk National University, Cheongju 28644, Republic of Korea. [5]Institute for Molecular Engineering, The University of Chicago, Chicago, IL 60637, USA. [6]Department of Chemistry, University of North Carolina at Chapel Hill, Chapel Hill, NC 27599, USA. [7]Department of Materials Science and Engineering, Northwestern University, Evanston, IL 60208, USA. [8]Research Resources Center, University of Illinois at Chicago, Chicago, IL 60607, USA. [9]Institute for Biophysical Dynamics, The University of Chicago, Chicago, IL 60637, USA.
*Corresponding author. Email: btian@uchicago.edu (B.T.); hgpark@korea.ac.kr (H.-G.P.); gaoxiang6803@gmail.com (X.G.)
†These authors contributed equally to this work.

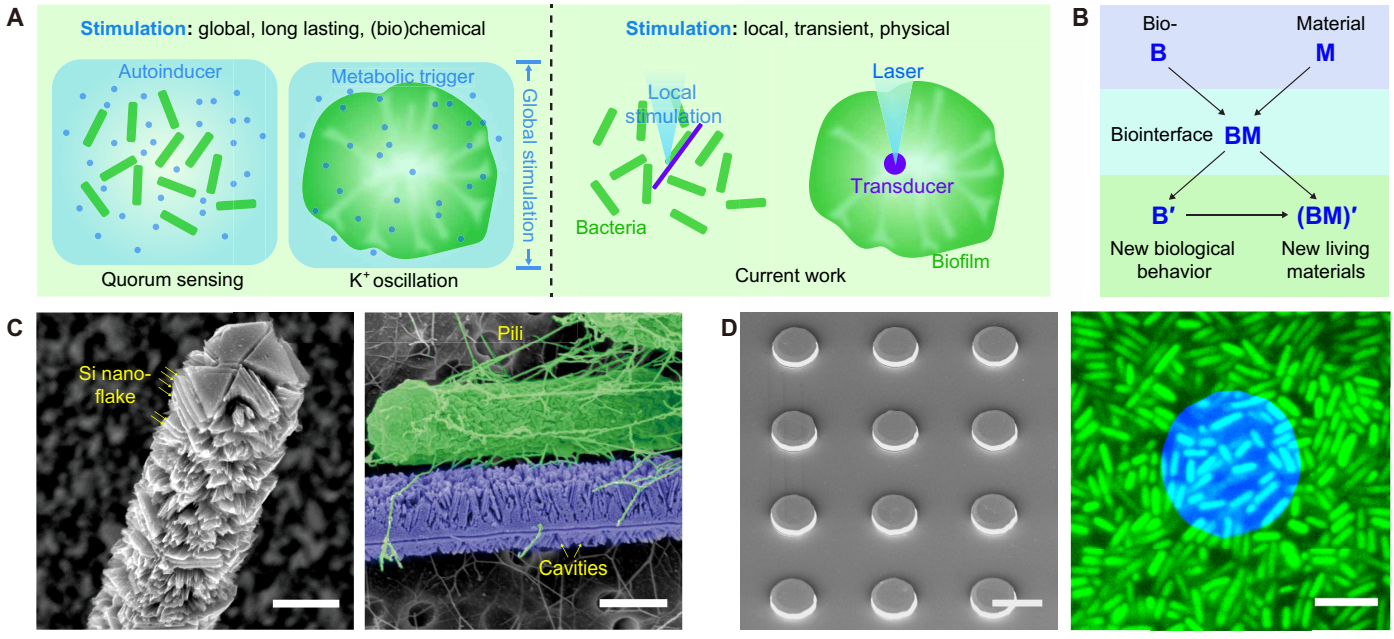

Fig. 1. Structured Si for multiscale interfaces with microbial systems. (**A**) A schematic diagram illustrating the advantage of material-based optical stimulation tools for the study of transient bacterial signaling. Existing tools are only suitable for the study of prolonged and large-scale bacterial communications, e.g., quorum sensing and K^+ signaling, due to their induction of slow or global changes in a microbial environment. Optical modulation techniques, using nongenetic transducers, can introduce local, transient, and physical perturbations to the microbial community. These new platforms have the potential to uncover transient microbial signaling. (**B**) Schematic illustrating the utility of interfacing biological systems with functional materials. Such biointerface not only allows the probing of new biological behaviors but also creates new opportunities to form dynamic hybrid living matters. (**C**) SEM image of a mesostructured Si nanowire (left) synthesized via chemical vapor deposition (CVD) and subsequent defect-selective wet etching. Pseudocolored SEM image (right) showing that the nanowire (purple) scale is similar to that of a bacterial cell (green). The rough surface topography of the nanowire can be well anchored by the bacteria pili. Scale bars, 0.5 μm. (**D**) SEM image (left) of 2D Si discs (~2-μm thickness) made from top-down fabrications. Overlaid confocal microscope image (right) showing an Si disc (blue) on the top of a *B. subtilis* biofilm (green) after 1 day of coculture. Bacteria were stained with LIVE/DEAD bacterial viability kit. Scale bars, 10 μm (left) and 5 μm (right).

roughness (Fig. 1C and figs. S1 and S2). Scanning electron microscopy (SEM) images of Si nanowire/bacteria junctions revealed that the cavities from the mesostructured Si could serve as anchoring points for the bacterial pili (Fig. 1C and fig. S3).

For interfaces with quasi-2D biofilms (fig. S4), we selected Si microplates (Fig. 1D). Using top-down microfabrication on silicon-on-insulator (SOI) wafers, we built a broad spectrum of Si microplates that were ~2 μm in thickness, with defined shapes (e.g., circles, squares, triangles, and crescents) (fig. S5). These geometry variations with deterministic properties are essential to mechanistic studies of biofilm signaling. Biofilms cultured over Si microplates were healthy and continuous (Fig. 1D). To manipulate the macroscopic activities of biofilms, we constructed centimeter-scale Si meshes (fig. S6). With the open network design, the mesh can conform to the surface of a mature biofilm and integrate seamlessly with individual cells following coculture (fig. S6).

Beyond dimension-matched interfaces (*19*), Si materials need to effectively transduce light energy into localized signals that cells can respond to, especially given that no genetic modification is used here to enable light sensitivity in bacteria. We used a previously described patch-clamp setup (*22*) to assess the photoresponses of different Si structures (fig. S7). Representative current dynamics (Fig. 2A) recorded from a mesostructured Si nanowire showed that it generated a ~4.1-K increase in the local temperature (pipette tip ~5 μm above the nanowire center) from a 1-ms laser pulse with negligible photoelectrochemical responses (Fig. 2A and fig. S7). In contrast, a smooth nanowire can only heat up the surrounding medium by ~1.1 K (fig. S7). Nanowires with different roughness have quite narrow temperature distributions, suggesting a good uniformity of the materials (fig. S8). Consistent with previous studies on mesoporous Si (*17*, *30*), the hierarchical cavities in the mesostructured nanowire likely contribute to enhanced light absorption, reduced thermal conductivity, and reduced heat capacity of Si. According to the Fourier thermal conduction equation, these trends will lead to its enhanced photothermal response in the mesostructured nanowire, which was also confirmed by finite element simulation (fig. S9).

We first studied the Si nanowire–enabled transient photothermal effect on planktonic cells. Si nanowires were placed in a suspension of *Escherichia coli* and illuminated by laser pulses (592 nm, ~8.28 mW, ~500-nm spot size, 1 ms). The pulses evoked an instantaneous bacterial attraction to the nanowire surface, collecting cells from a region of 10 μm within ~250 ms (Fig. 2B). Although the light pulse was transient, bacterial cells stuck to the nanowire surfaces for at least 10 min (fig. S10), likely due to the strong interaction between the mesoscale cavities and the bacterial pili. The total number of collected bacteria increased with repetitive illuminations at the same nanowire location (Fig. 2B). When the laser spot was swept along the same nanowire, the original bacteria/Si junction broke and reformed at the new illumination center (fig. S11). The cells were alive throughout these transient optical manipulations (fig. S12). Gram-positive *Bacillus subtilis* were attracted to the nanowires in a manner similar to that of the Gram-negative *E. coli* (fig. S13). Moreover, polystyrene

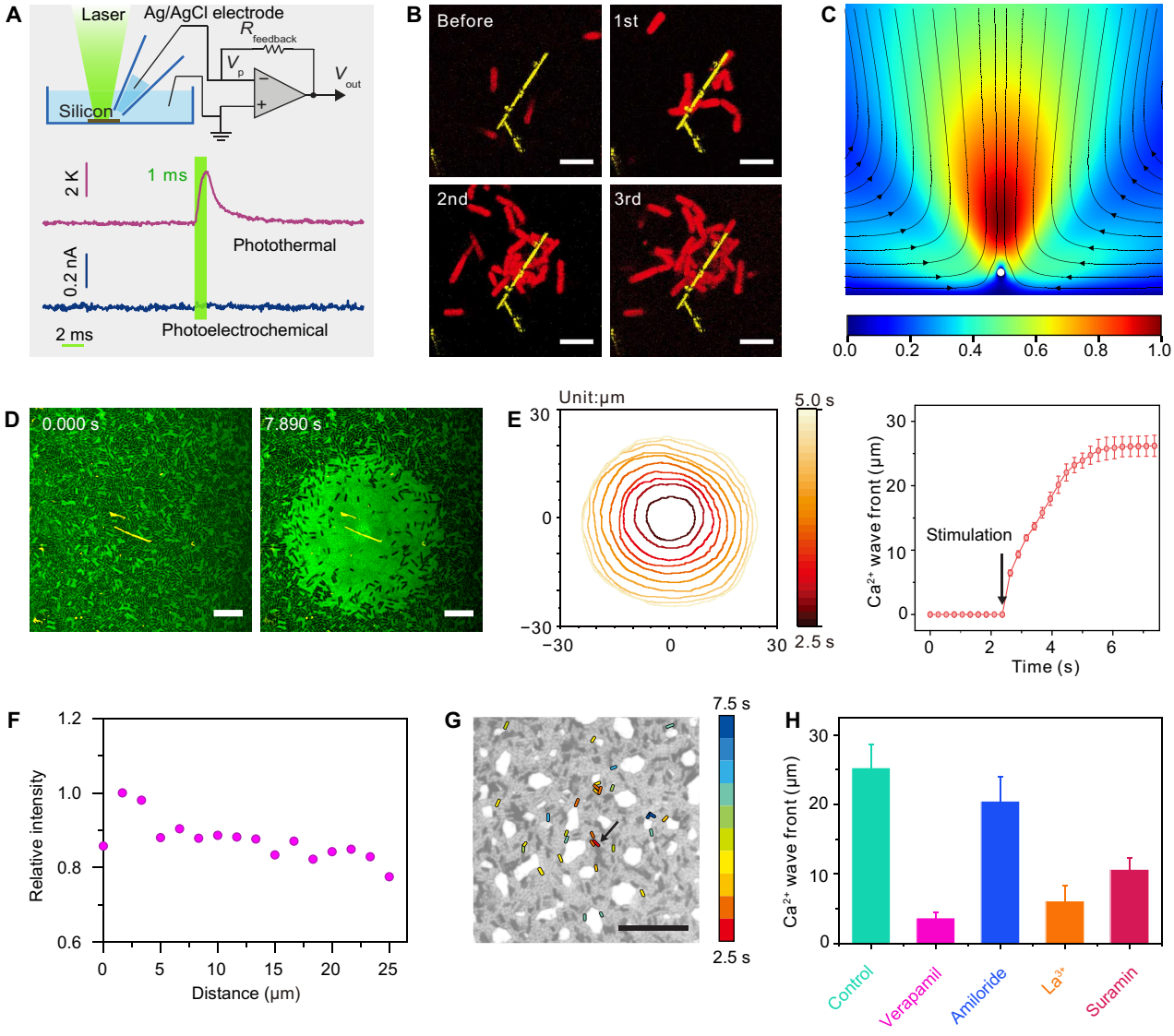

Fig. 2. Si nanowires can manipulate both single cell and biofilm activities. (**A**) Experimental setup for the photoresponse measurement of Si nanowire with representative traces of local temperature (upper) and photocurrent (lower) dynamics of a mesostructured Si nanowire in response to laser illumination (532 nm, ~5-μm spot size, 60.1 mW for 1 ms). Green-shaded area highlights the laser illumination period. (**B**) Bacterial cells from the suspension are repeatedly attracted onto the Si nanowire upon light stimulation. Red, *E. coli* expressing eforRed; yellow, Si nanowire scattering. Scale bars, 5 μm. (**C**) FEA simulation of convective water flow velocity distribution with the speed (map) and the directions (arrows) near the laser illumination spot on the Si nanowire; white dot represents Si nanowire (cross section). (**D**) Confocal microscope images of light-induced Ca^{2+} elevation in a *B. subtilis* biofilm before (left) and after (right) stimulation (592 nm, ~22.3 mW, 1 ms). Green, Ca^{2+} fluorescence; yellow, nanowire scattering. Scale bars, 10 μm. (**E**) Ca^{2+} wave propagation after laser stimulation. Left: Contour plot showing the propagation of the Ca^{2+} wave front over time. (0, 0) coordinate denotes the laser illumination spot. Right: Radial average Ca^{2+} propagation profile showing activation up to ~26.3 μm from the center with a ~7.63-s time delay. Error bars denote SDs. (**F**) Ca^{2+} fluorescence intensity along the radial direction shows only slight signal decay within the propagation range. (**G**) Color-coded map showing the jumping activation of non-neighboring cells. Ca^{2+} signaling was initiated from the laser spot (back arrow, at $t = 2.5$ s) and then propagated to adjacent bacterial cells (up to $t = 7.5$ s). The color code indicates the time scale. Gray cells did not show fluorescence intensity change after the stimulation. Scale bar, 20 μm. (**H**) Statistical analysis of the Ca^{2+} propagation distances using different inhibitors. $n = 5$ for control, $n = 6$ for verapamil, $n = 4$ for amiloride, $n = 6$ for La^{3+}, and $n = 4$ for suramin. Error bars denote SDs.

beads ~1 μm in diameter, a comparable size to bacteria, were also be attracted regardless of positive or negative surface charge (fig. S14).

The experimental results proved that the nanowire-based cellular positioning was not driven by specific biological process or electrostatic interaction. We hypothesized that the establishment of a temperature gradient near the illuminated spot and the corresponding convective flows of the medium around the nanowire may be responsible for the observed cellular attraction, in a similar fashion with previous reports on photothermal trapping of particles (*31*–*34*). Finite element analysis (FEA) of the light-induced temperature field and fluidic dynamics confirmed that the thermal gradient–induced convective flows laterally collected bacterial cells toward the nanowire to establish cell/Si junctions through pili/cavity interactions (Fig. 2C and fig. S15). Since the collection process is purely physical, this

method may be broadly used for single bacterial cell trapping and subsequent analysis.

Given the critical role of calcium ions (Ca^{2+}) as a secondary messenger in key physiological responses of the mammalian system cell physiology (e.g., proliferation, differentiation, and survival) (*35*) and the recent discovery of induced Ca^{2+} signal propagation in plants (*36*), we stained planktonic *B. subtilis* cells with a Ca^{2+} indicator Fluo-4 acetyloxymethyl ester (Fluo-4 AM) and illuminated a nanowire with a laser pulse (592 nm, ~8.28 mW, ~500-nm spot size, 1 ms). Immediately following the cell trapping onto the nanowire, the intracellular Ca^{2+} fluorescence intensity was raised (fig. S16), suggesting a possibility of induced Ca^{2+} signaling in bacterial community.

To test this hypothesis, we then applied Si nanowires to cultured *B. subtilis* biofilms and probed Ca^{2+} signaling upon Si nanowire–assisted local optical stimulation (592 nm, ~22.3 mW, ~500-nm spot size, 1 ms) in the middle of a time-lapse calcium imaging series. Notably, we observed a fast Ca^{2+} wave initiated from the bacterial cells near the nanowire under stimulation (Fig. 2D, fig. S17, and movie S1). Although transient (i.e., 1 ms) local heat shock may be responsible for the initial Ca^{2+} surges around the center, the Ca^{2+} wave extended to distal cells (~26.3 μm away from the stimulation spot) with a much longer lag time after the illumination (i.e., ~7.63 s). The three-orders-of-magnitude discrepancy between the heating period and the recorded signaling duration strongly indicates the existence of intercellular communication across the biofilm (Fig. 2E). Line profiles of the Ca^{2+} intensity along radial directions showed only modest signal decays, suggesting the involvement of active processes with local amplifications during the propagation (Fig. 2, E and F) (*2*). Using a cellular automation model that assumes bacterial cells can only reach one of two possible stationary states: refractory or permanently activated, we were able to simulate this uniform distribution in a simple active signaling model (fig. S18). The Ca^{2+} wave propagation is unprecedented in any biofilms studied so far, and the average propagation rate of ~8.3 $\mu m\ s^{-1}$ is even comparable with that of a mammalian cell culture (*37*). In the absence of either Si nanowires or optical stimulation, no induced Ca^{2+} signaling was observed (fig. S19). When the biofilm was not completely intact, the Ca^{2+} signaling still occurred, but with a "jumping" activation pattern (Fig. 2G). Both intact and broken biofilms can carry rapid calcium propagation. However, the different mode of transport (e.g., continuous versus jumping) suggests that the biofilm structure may be critical for signal propagation. *B. subtilis* expressing the endogenous Ca^{2+}-sensitive protein (i.e., apoaequorin) also exhibited similar Ca^{2+} dynamics (fig. S20), which confirmed that the observed phenomenon was not due to the transport of fluorescence dye (i.e., Fluo-4 AM).

To identify the key components involved in this active and rapid signaling process, we added various inhibitors to the Si-bacteria coculture (Fig. 2H and fig. S21). For example, an adenosine triphosphate (ATP) receptor inhibitor, i.e., suramin, effectively reduced the propagation distance, highlighting ATP as a potential extracellular mediator during Ca^{2+} propagation. Plasma membrane ion channel blockers, including verapamil and lanthanum ions, terminated the Ca^{2+} wave propagation, which confirmed that the process indeed relied on ion channel activities. Given that the local heat-induced convective flow may also stimulate cells, we added the mechanosensitive ion channel blockers, i.e., amiloride, but saw no obvious blockage of the wave propagation. In addition, high-power stimulations did not cause any Ca^{2+} elevation at distal cells even with apparent biofilm deformation, further ruling out the possibility of mechanical stress–induced Ca^{2+} initiation and propagation (movie S2). Last, we also showed that Ca^{2+} signals can be evoked in other microbial species such as *Pseudomonas aeruginosa* (fig. S22) or *E. coli* through direct stimulation or interspecies communications (fig. S23), which suggested the generic nature of this type of Ca^{2+} signaling.

While the remotely controlled Si nanowire has contributed to the discovery of rapid Ca^{2+} signaling in biofilms, its 1D structure would limit the mechanistic studies of heat shock–induced Ca^{2+} signaling. For example, it is not clear if this process is due to the absolute temperature change (i.e., ΔT), the rate of temperature change (i.e., dT/dt), or even the spatial temperature gradient (i.e., dT/dr), because all these possible thermal effects have the maximum value at the nanowire locations where the Ca^{2+} signals were initiated. Therefore, we investigated which thermal effect induced the Ca^{2+} signaling process using a series of 2D Si microplates, whose shape and size could be precisely controlled (Fig. 3A and fig. S5). Similar to the nanowire, laser illumination at the center of a circular disc embedded in a *B. subtilis* biofilm instantaneously evoked Ca^{2+} wave propagation (Fig. 3, B and C, and movie S3). However, one key difference is that the Ca^{2+} propagation was not initiated from the stimulation site (i.e., the center of the disc). Rather, immediately following the laser illumination, the Ca^{2+} level of bacterial cells around the edge of the disc underwent a sharp elevation followed by bidirectional circular propagations toward the disc centroid and the biofilm outside the disc (Fig. 3C). A simple cellular automation model of an active signaling process qualitatively reproduced our experimental observations during the signaling process, i.e., active Ca^{2+} propagation from the disc edge and subsequent activation of cells at the centroid, whereas a purely diffusive model cannot explain the initiated signal from the edge could generate an isolated spot of Ca^{2+} signaling at the center (fig. S18).

Hypothesizing that the Ca^{2+} patterning was dependent on disc size, we performed the same experiment using Si discs with different lateral dimensions. Given the well-controlled fabrication and simple geometry of these Si materials, their photoresponses can be readily predicted by FEA and verified by patch-clamp recording, respectively (Fig. 3D and figs. S24 and S25). On the basis of Fourier's law of thermal conduction, as the size of the Si disc increases, laser-induced heat will be more distributed throughout the entire disc, resulting in a lower disc temperature. As such, the recorded local temperature near the patch pipette was inversely related to the disc size, i.e., a smaller disc induced a larger photothermal response (Fig. 3D). Correspondingly, the minimal laser power required to elicit the Ca^{2+} signaling gradually declined as the disc diameter decreased (Fig. 3E). Notably, even though Ca^{2+} signaling could be triggered using discs with all sizes (with corresponding minimal laser powers), the Ca^{2+} patterns were vastly different (Fig. 3G and fig. S26). For smaller Si discs (e.g., 10 or 20 μm in diameter), the elevated Ca^{2+} spots (i.e., the "excited" cells) were predominantly outside the discs up to ~6 μm from the edges; on the other hand, larger Si (e.g., 60 or 80 μm in diameter) generated a bimodal Ca^{2+} distribution with peaks near both the disc centers and the edges. Once the Ca^{2+} wave stopped propagating, the Ca^{2+} pattern was stable for at least 5 min (fig. S27). In all these experiments, cell death was negligible (fig. S28), consistent with the observed cell viability from single-cell manipulation experiments (fig. S12).

The Si disc size–dependent Ca^{2+} patterning implied that the key factor in Ca^{2+} activation was more than just the absolute temperature change (i.e., ΔT). To unravel the possible mechanism, we again performed FEA to map the spatiotemporal dynamics of the entire

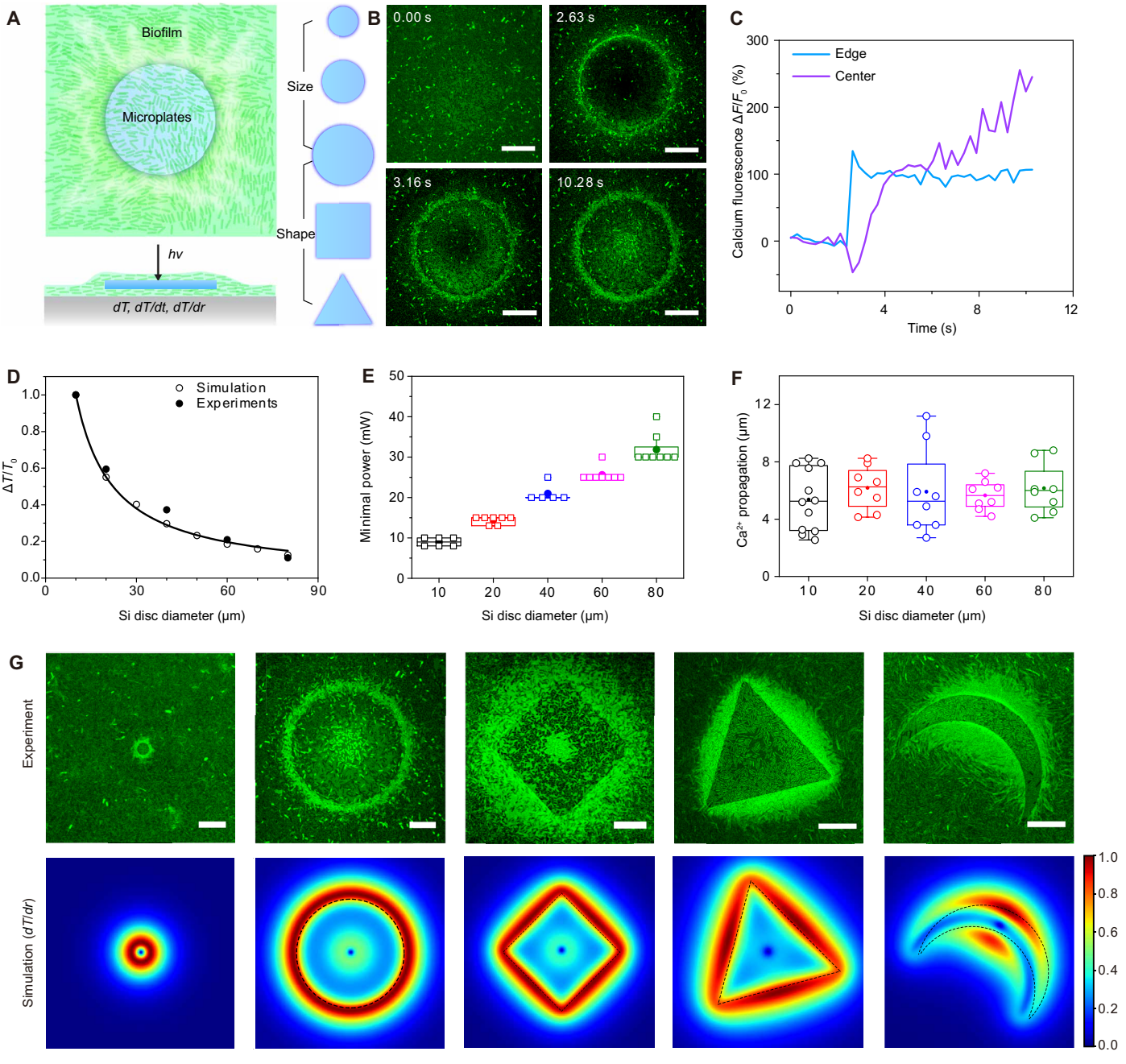

Fig. 3. Si microplates permit mechanistic study of rapid Ca^{2+} signaling in biofilms. (**A**) Schematic illumination of Ca^{2+} signaling propagation mechanism stimulated by Si microplates. Si microplates with different sizes and various shapes were designed to investigate the stimulation mechanism. Absolute temperature (ΔT), temporal gradient of temperature (dT/dt), and spatial gradient of temperature (dT/dr) are three possible factors. (**B**) Confocal microscope time series showing the evolution of Ca^{2+} distribution over time. Upon light illumination at the center of the disc, cells near the disc edges first experienced intracellular elevations followed by bidirectional circular propagation toward the disc centroid and the rest of biofilm outside the disc. The laser (592 nm, ~32.2 mW) was on for 1 ms right before the time point of 2.63 s. Scale bars, 30 μm. (**C**) Quantitative analysis of the fluorescence intensity of Ca^{2+} over time showing the immediate Ca^{2+} activation near the disc edge and a delayed onset near the disc center. The initial dip of the fluorescence intensity near the center is likely due to photobleaching by the stimulation laser. (**D**) FEA simulation (unfilled circles) and patch-clamp recording (filled circles) show an inverse relationship between the disc size and the photothermal effect. Numerical fitting of the simulated data points is plotted. (**E**) Minimal power required to evoke the Ca^{2+} signaling in biofilm gradually increases with larger discs. (**F**) Ca^{2+} propagation distances outside the discs are almost identical in all cases using the minimal powers required to elicit Ca^{2+} signaling. (**G**) Recorded final Ca^{2+} distribution patterns and simulated spatial gradient of temperature right after stimulation correlate well with each other for Si microplates of different sizes and geometries. Scale bars, 20 μm.

photothermal process (Fig. 3G and figs. S26 and S29). Upon illumination at the center of the disc, although the absolute temperature (i.e., ΔT) and the rate of temperature change (i.e., dT/dt) were always highest at the center, the spatial gradient of the temperature distribution (i.e., dT/dr) actually peaked near the edge due to the large mismatch between the thermal conductivities of Si and the medium (figs. S26 and S29). The fact that Ca^{2+} initiation always occurred at the disc edges suggested that dT/dr, rather than ΔT or dT/dt, was responsible for Ca^{2+} initiation.

Furthermore, the dT/dr profile correlated highly with the static Ca^{2+} distribution, which could possibly explain the observed size-dependent Ca^{2+} patterns (fig. S26). For example, in a large-sized Si disc, temperature will first undergo an exponential decay from the heat source (i.e., the center of the disc under illumination) to the edge, followed by another substantial temperature drop at the Si/medium interface due to the large interfacial thermal resistance and the poor thermal conductivity of water. As a result, a bimodal time-dependent dT/dr distribution can be perceived, which is similar to the static Ca^{2+} pattern (fig. S26). In a smaller Si disc, however, heat is more uniformly confined within the disc such that only one major dT/dr peak is expected at the edge of the disc (fig. S26). In both scenarios, the dT/dr profiles are more or less the same in the regions outside the discs, consistent with the observation that maximum Ca^{2+} propagation to the rest of the biofilm (fig. S26) always stayed at the similar level (i.e., ~6 μm from the disc edge under the current illumination condition) (Fig. 3F). This thermal gradient sensing is reminiscent of results from previous studies in which bacteria responded to the chemical gradient rather than the absolute chemical concentration (*38*), although the response time was quite different, i.e., milliseconds in our observation versus seconds in previous studies. To further support our model of dT/dr-dependent Ca^{2+} signaling, we conducted additional FEA and Ca^{2+} imaging using Si with a variety of shapes, e.g., triangle, square, and crescent, which consistently yielded good agreements between the simulated patterns and the experimental observations (Fig. 3G and fig. S30).

Besides studying the principles that governed the Ca^{2+} activation and wave propagation, we were also interested in the aftermath of this signaling cascade and its impact on the biofilm. To this end, we sequentially increased the stimulation power on the same Si disc and monitored the induced Ca^{2+} patterns (fig. S31 and movie S4). Initially, both the intensity and area of the Ca^{2+} fluorescence continued to increase with higher laser powers. At a threshold point, the Si disc was instantaneously kicked away (likely due to the photothermally induced convective flow or shock wave), taking the overlapping cells with it, presumably due to the strong interfacial adhesion. Notably, surrounding cells that experienced the stepwise Ca^{2+} elevation were also spontaneously stripped off the biofilm. On

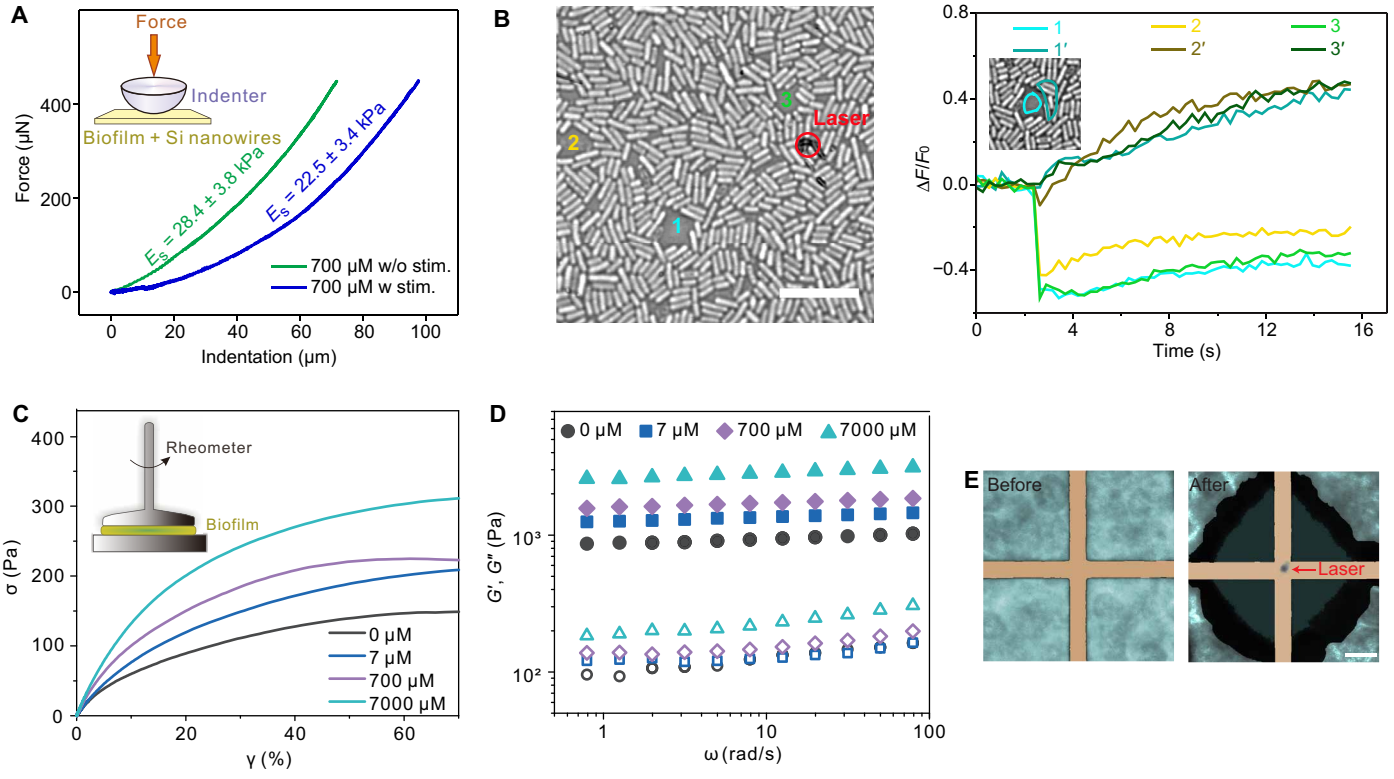

Fig. 4. Chemical-mechanical coupling exists in biofilms. (**A**) Representative force-indentation depth curves from spots with and without laser stimulation, respectively (within the same biofilm). Biofilms were cultured in normal MSgg agar medium containing 700 μM Ca^{2+}. (**B**) Confocal bright-field image showing a biofilm with several cell-free spots (left). Red circle indicates the laser stimulation. Scale bar, 10 μm. Quantitative analysis of the fluorescence intensities (right) taken from the extracellular spaces (1, 2, and 3) and the surrounding cells (1′, 2′, and 3′). Right after the laser stimulation, the extracellular spaces showed an immediate decrease in fluorescence, whereas the surrounding cells showed rapid increases, indicating that Ca^{2+} moved from the extracellular matrix to the intracellular space. (**C**) Stress-strain curves of biofilms cultured from MSgg agar medium with various Ca^{2+} concentrations. (**D**) Dynamic modulus measurements show a similar trend of Ca^{2+}-dependent storage and loss moduli changes in biofilms. Solid symbol: G', storage modulus; open symbol: G'', loss modulus. (**E**) Pseudocolored microscope images of biofilm before and after laser stimulation. Upon high-power laser stimulation, the biofilm was disrupted effectively. Cyan, biofilm; salmon, Si mesh. Scale bar: 10 mm.

the other hand, when we directly illuminated the Si disc using the threshold laser power without any prior low-power stimulations, only the disc and its overlapping cells were removed (fig. S32). In the latter case, there was negligible Ca^{2+} wave propagation before the disc left the biofilms. To summarize, even if the final stress (i.e., the input thermal energy) on the biofilm remained the same, the cell loss was much larger with prior Ca^{2+} signal propagation. Considering that the pressure force exerted by the Si disc and the medium flow are solely dependent on the laser power (fig. S31), we hypothesized that the biofilm's intrinsic mechanical properties (e.g., stiffness, viscoelasticity) changed after the Ca^{2+} propagation. This seemingly unexpected chemical-mechanical coupling may be crucial to bacterial response under stressful conditions.

To test our hypothesis, we first used nanoindentation to directly measure the stiffness of the same biofilm at different locations with and without Ca^{2+} signaling (Fig. 4A and fig. S33). In accordance with our hypothesis about the potential coupling between Ca^{2+} and biofilm mechanics, the laser-stimulated part of the biofilm indeed exhibited a marked drop in stiffness (reduced by 20.8%) compared with the unstimulated one (fig. S33). Furthermore, we also observed completely opposite trends in Ca^{2+} intensity between the extracellular (sharp decrease) and intracellular (steady increase) spaces after light stimulation (Fig. 4B), indicating that rapid movement of extracellular Ca^{2+} to the intracellular space may be responsible for biofilm weakening. To further understand this phenomenon, we performed multiple bulk tests of biofilms cultured in agar medium with various Ca^{2+} concentrations (fig. S34). Using a dynamic shear rheometer, the shear modulus (G as a measure of rigidity) from stress-strain curves and the storage (G' as a measure of elasticity) and loss (G'' as a measure of viscosity) moduli from dynamic modulus measurements all showed a consistent trend that the biofilm moduli decreased drastically when the extracellular Ca^{2+} level was low (Fig. 4, C and D). Given that the most abundant component in the biofilm extracellular substances is alginate-based polysaccharides (*39*), it is expected that the biofilm behaved similarly to ionically cross-linked alginate hydrogels, whose mechanical properties are also highly dependent on Ca^{2+} concentrations (fig. S34). Nevertheless, the ability of bacterial cells to dynamically respond to local stimuli and actively modulate their mechanical properties is unique to the living biofilm system as the abiotic hydrogels do not confer such a feature. It also implies that sequential stimulation may represent an effective method to optically destroy biofilm, instead of a one-time high-power ablation, as demonstrated in Si mesh (Fig. 4E) interfaced biofilms.

DISCUSSION

Using optically actuated multiscale Si structures, we have revealed several thermal gradient–based transient, rapid, and integrated signal transductions in microbial systems (Fig. 5). Unlike existing biochemical and genetic toolboxes that target cell populations, this highly localized physical approach enabled control of bacterial behaviors (e.g., single-cell manipulation) and the discovery of fast Ca^{2+} signaling in biofilms. Upon external thermal shock via laser illumination onto the Si materials, bacterial cells sense the thermal gradient, and those close to the largest gradient are activated. During the subsequent active propagations, Ca^{2+} in the surrounding extracellular substances fluxes into the intracellular spaces, and the local biofilm modulus correspondingly reduces. Currently, the exact molecular understanding of this calcium signaling pathway is still lacking, mostly because that our highly localized and transient photostimulation method is not fully compatible with existing biochemical tools, such as mass spectroscopy. More macroscopic experiments with genetic manipulation need to be conducted to screen possible signaling pathways.

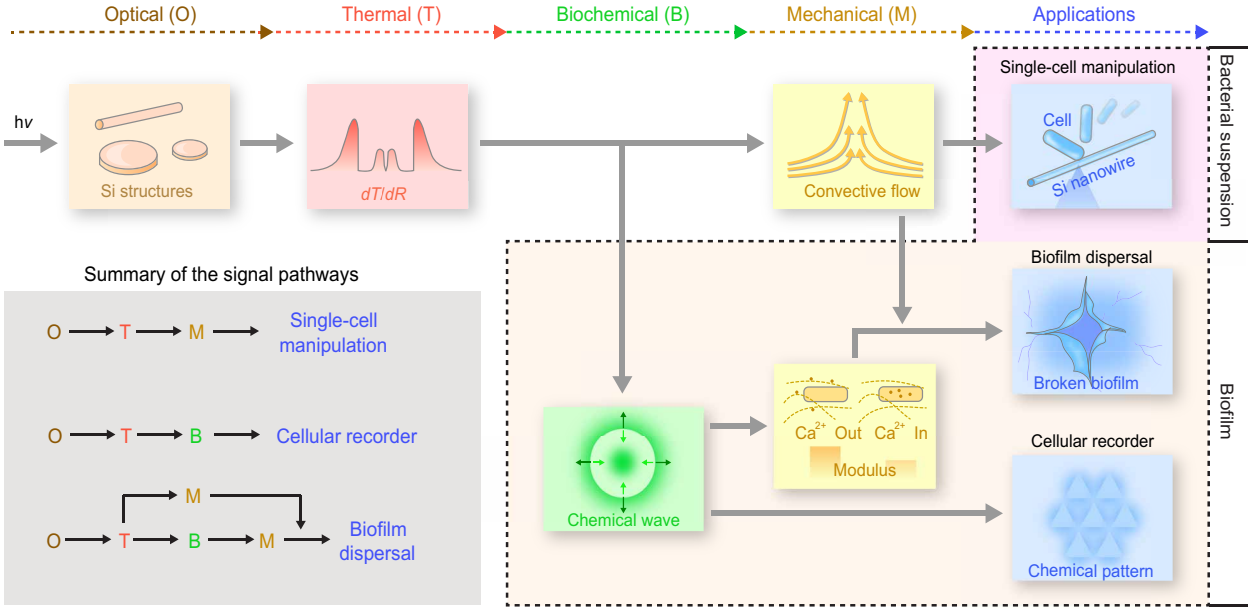

Fig. 5. Summary of multiscale Si structures for microbiology studies and bioengineering applications. Optically controlled Si structures output transient thermal signals. Resulting thermal spatial gradients are sensed by bacteria, triggering rapid intercellular signaling. In addition to the fundamental studies, our Si-bacteria platform will enable a wide spectrum of applications including single-cell manipulation based on photothermally induced convective flows, cellular recording of chemical patterns based on the temperature-gradient Ca^{2+} activation, and biofilm disruption based on chemical-mechanical coupling.

On the other hand, the seamless integration of synthetic Si materials with living biological systems also permits a wide range of bioengineering applications. For example, even though the total duration of *dT/dr* dynamics (fig. S29) is much shorter than that of Ca^{2+} propagation (i.e., millisecond scale versus second scale), biofilms can still "record" the transient thermal gradient patterns in the form of long-lasting Ca^{2+} patterns, similar to sequential exposure and development procedures in the photographic processing. Thus, dynamically programmed Ca^{2+} redistribution, triggered by optical inputs, represents a straightforward method of imprinting custom-designed spatiotemporal patterns onto living systems (Fig. 5 and fig. S35). Coupled with other platforms, such as microfluidic (fig. S36) and microscopy, our Si-based optical modulation may be further extended to the study of other possible signaling pathways, e.g., potassium dynamics (fig. S37). Notably, the potassium propagation requires a much higher laser power compared with calcium (79.5 mW versus 22.3 mW), and was likely coupled with membrane potential changes, in consistency with previous reports (*2*, *4*). The roles and differences between potassium and calcium signaling need to be further studied. In this work, we used the photothermal effect of the material, and only one physical stress was presented. In the future, other types of physical insults, such as electrical and mechanical inputs, may be enabled by other material platforms toward multimodal interrogation of the microbial system. Together, our results suggest that a tightly regulated system with integrated signal transductions (e.g., optical ➔ thermal ➔ biochemical ➔ mechanical) may be constructed as hybrid living matters toward future synthetic biology and adaptable materials.

MATERIALS AND METHODS

Si nanowire synthesis

Coaxial Si nanowires were synthesized as described (*18*, *22*) using an Au-catalyzed chemical vapor deposition (CVD) process. First, Si (100) substrates (NOVA Electronic Materials, *n*-type, 0.001 to 0.005 ohm·cm) were coated with 100-nm Au colloidal nanoparticles (Ted Pella) and loaded into the CVD chamber. Second, silane (SiH_4) was introduced to the reactor subsystem as a gaseous precursor for the growth of Si nanowires, and hydrogen (H_2) was used as the carrier gas. SiH_4 and H_2 were delivered at 2 and 60 standard cubic centimeters per minute (sccm), respectively, for the formation of intrinsic Si nanowire core (*i*-core). During the core synthesis, the system was maintained at 470°C under a pressure of 40 torr for 15 min. Then, the growth was paused in an H_2 flow of 60 sccm at 15 torr for around 15 min, during which the CVD furnace temperature was raised to 650°C in preparation for the subsequent intrinsic shell (*i*-shell) deposition. The *i*-shell growth was carried out at 650°C at a pressure of 15 torr for 30 min with either low or high flow rate. For the low flow rate, SiH_4 and H_2 were delivered at 0.3 and 60 sccm, respectively. Otherwise, SiH_4 was increased to 1 sccm in the high flow rate synthesis of the shell. Subsequent wet chemical etching (*29*) of the nanowire was performed at room temperature to selectively Si etch from grain boundaries in a mixed solution constituting of 0.15 M $K_2Cr_2O_7$ and 49% hydrogen fluoride (HF) (v/v 1/2) for 30, 60, and 120 s, respectively.

Fabrication of Si microplates

The Si microplates were fabricated according to published procedures (*18*, *22*). Briefly, SOI wafers were first treated with mild O_2 plasma of 100 W for 1 min and then spin coated with MCC primer (MicroChem primer 80/20) under 500 rpm for 5 s and then 3000 rpm for 30 s to promote the adhesion between the wafer and the subsequent photoresists layer. Then, a layer of SU-8 2005 negative photoresist was spin coated with the same protocol (500 rpm for 5 s and then 3000 rpm for 30 s). The wafer was baked at 65°C for 2 min and then at 95°C for 2 min before being patterned with a standard photolithography process under an ultraviolet (UV) light exposure power of 200 mJ/cm^2. After the UV exposure, the wafer was baked again at 65°C for 2 min and then at 95°C for 2 min and was then developed in the SU-8 developer for 1 min. The as-patterned substrate was rinsed with acetone, isopropanol, and deionized (DI) water, followed by a hard bake process under 180°C for 20 min to improve its stability under the reactive ion etcher [RIE; Oxford Instruments, PlasmaPro NGP80 inductive-coupled plasma (ICP)]. The RIE completely etched the unprotected Si layers with CF_4 (45 sccm) and Ar (5 sccm) under 100-W radiofrequency power and 400-W (ICP) power. The RIE-etched patterns were first treated with a piranha solution (volume ratio H_2SO_4:H_2O_2 = 3:1) at room temperature for 4 hours to etch the SU-8 protection layer and remove other organic contaminants. The wafer was, lastly, treated with 49% HF overnight to release the patterned Si by etching off the underneath oxide layer.

Si photoresponse measurements

The photoresponse measurements were conducted according to published procedures (*22*). Briefly, a standard patch-clamp setup was used. An upright microscope (Olympus, BX61WI) with a 20×/0.5 numerical aperture water immersion objective was used to deliver light pulses from a laser (Laserglow, 532 nm, diode-pumped solid-state laser; spot size, ~5 μm). The light pulses were controlled by transistor-transistor logic (TTL) signals (1 ms) delivered from a digitizer (Molecular Devices, Digidata 1550). Voltage-clamp protocols were done by an Axopatch 200B amplifier (Molecular Devices) controlled by the pCLAMP software (Molecular Devices). Glass pipettes were pulled in a Flaming/Brown-type micropipette puller (Sutter Instrument, P-97) for a final resistance of ~1 megohm when filled with 1× phosphate-buffered saline (PBS, Thermo Fisher Scientific) solution. In a typical measurement, an Si material was immersed in the same PBS solution, where the pipette tip was positioned in close proximity to the Si surface (~5 μm). The ionic currents across the pipette tip were recorded in the voltage-clamp mode, where the holding levels of the pipette were adjusted using the pipette offset knob. After the photoresponse measurement, the same micropipette was placed into another dish of preheated PBS with an initial temperature of about 50°C. A thermocouple was positioned close to the pipette tip during the temperature measurement. A calibration curve was created on the basis of the pipette resistance changes in the range between 50° and 20°C, which was then used to estimate the local temperature increase.

Bacteria strains and plasmids

Bacteria strains and plasmids used in this work are listed in table S2. *E. coli* DH5α was used for plasmid construction and bacterial cells attraction. *E. coli* was grown in Luria-Bertani (LB) medium at 37°C with supplement of ampicillin (Amp, 100 μg/ml). *P. aeruginosa* P2 and pSY1064 containing expressed eforRed fluorescence protein were offered by J. C. Alverdy (The University of Chicago) and G.-P. Zhao (Chinese Academy of Sciences), respectively. *B. subtilis* strains NCIB 3610 and pSG1154 were purchased from the Bacillus Genetic Stock Center.

Growth condition

The *B. subtilis* biofilms were grown in MSgg minimum medium (*2*) agar plate, which contains 5 mM potassium phosphate buffer, 100 mM Mops buffer (pH 7.0 adjusted with NaOH), 2 mM $MgCl_2$, 700 μM $CaCl_2$, 50 μM $MnCl_2$, 100 μM $FeCl_3$, 1 μM $ZnCl_2$, 2 μM thiamine hydrochloride, 0.5% (v/v) glycerol, 0.5% (w/v) monosodium glutamate, tryptophan (50 μg/ml), and phenylalanine (50 μg/ml). Typically, the *B. subtilis* biofilms were incubated at 30°C for 2 days, and then Si materials were added to the biofilm and continuously grown overnight before usage. For the cross-species Ca^{2+} signaling experiment, the *B. subtilis* biofilms were, firstly, incubated at 30°C for 2 days before introducing the *E. coli* containing expressed aforRed into the biofilm, and then the coculture was grown overnight before the experiments. *P. aeruginosa* P2 biofilms were grown in Tryptic Soy Broth supplemented with 0.2% (w/v) glucose and were incubated at 37°C for 2 days before the laser stimulation experiments.

Construction of the apoaequorin expression vector for *B. subtilis*

Plasmid pSG1154-apoaequorin was constructed using GeneArt Seamless Cloning and Assembly Kit (Life Technologies). Briefly, the encoding gene for the apoaequorin fragment (*40*) was chemically synthesized by GenScript, followed by assembling to the pSG1154 vector. The construction was confirmed by sequencing and then integrated into the wild-type *B. subtilis amyE* locus of chromosome using the standard transformation method (*41*).

In vivo reconstitution of apoaequorin

The suspension of *B. subtilis*–expressing apoaequorin was incubated for 4 to 5 hours in darkness with 2.5 μM coelenterazine in MSgg medium at 37°C (*42*). The relative light emission was measured using a fluorometer, while 7 mM Ca^{2+} was added during the measurement.

Single-cell manipulation

The overnight LB-cultured *E. coli* or *B. subtilis* was diluted to OD_{600} = 1 and mixed with mesostructured intrinsic nanowires. The solution was added on a FluoroDish (World Precision Instruments) and covered with a coverslip. The single-cell manipulation was performed using a confocal laser scanning microscope (Leica, SP5 II STED-CW). In a typical experiment, a laser pulse (1 ms, 592 nm) was delivered to a nanowire/bacterial cell of interest in the middle of an imaging time series.

Nanoparticle manipulation

Carboxyl-terminated fluorescent Nile red polystyrene particles (1% w/v, 0.84 μm, Spherotech) were diluted by 1:50 in DI water. Amino-terminated fluorescent yellow particles (1% w/v, 0.81 μm, Spherotech) were, firstly, diluted by 1:50 in 0.1% poly-L-lysine (PLL), followed by incubation for 1 hour. Then, the solution was centrifuged at 5000 rpm for 5 min and resuspended with the same volume of DI water. Zeta potential measurements on a Zetasizer (Malvern Nano ZS) confirm that the carboxyl fluorescent Nile red particles and PLL-treated amino fluorescent yellow particles have negative and positive charges on the surfaces, respectively. The particles were then mixed with intrinsic nanowires, and 10 μl of the mixture was added on a FluoroDish Cell Culture Dish (World Precision Instruments) and covered with a coverslip. The single-particle manipulation was performed using the same Leica SP5 confocal microscope. In a typical experiment, a laser pulse (1 ms, 592 nm) was delivered to spots of interest in the middle of an imaging time series.

Electron microscopy

Si materials including intrinsic nanowires, microplates, and meshes were imaged with a SEM (Carl Zeiss, Merlin) directly. The bacteria and nanowire mixture after laser illumination or the biofilm samples were firstly fixed in 4% paraformaldehyde, followed by washing in DI water and being dehydrated with an increasing ethanol gradient. The samples were dried in a critical point dryer (Leica EM CPD300) and imaged under the same SEM. Transmission electron microscopy (TEM) was performed on both FEI F30 and JEOL JEM-3010. Nanocrystalline Si nanowires were sonicated in isopropanol (Sigma-Aldrich, USA) and then dispersed over copper grids (Ted Pella Inc., Lacey Formvar/Carbon, 200 meshes) for cross-sectional imaging and selected area electron diffraction. The cross sections of the nanowires were prepared by ultramicrotomy. More specifically, Si nanowires were embedded in epoxy resins, which were then solidified at 60°C for 24 hours. Thin epoxy sections of ~100 nm were cut using an ultramicrotome (Ultracut E, Reichert-Jung), collected on lacey carbon grids (Ted Pella Inc.), and imaged using TEM.

Calcium imaging

The *B. subtilis* biofilm, the *P. aeruginosa* P2 biofilm, or the *E. coli*–*B. subtilis* cocultured biofilm was first transferred onto FluoroDish Cell Culture Dishes (World Precision Instruments). Intrinsic nanowires or Si discs were either added into the culture medium or drop casted onto the biofilm and then cocultured overnight. The cocultured bacteria (with Si materials) were stained with 10 μM Fluo-4 AM (Life Technologies) for 1 hour at 37°C. Inhibitors were added at their indicated concentrations [100 μM verapamil, 100 μM amiloride, 5 mM lanthanum(III), and 100 μM suramin] when needed. The stained biofilms were imaged using the Leica SP5 confocal microscope. For all the intrinsic nanowire stimulation experiments, a laser pulse (592 nm, 1 ms, ~22.3 mW) was delivered to the nanowire/biofilm interface of interest in the middle of a calcium imaging time series. For the Si disc stimulation experiments, discs were illuminated by stepping the laser power from ~2.09 to ~42.7 mW (592 nm, 1 ms) to the center of the Si discs of interest. The cellular fluorescence intensity over time was analyzed using the ImageJ software (National Institutes of Health).

Potassium imaging

B. subtilis biofilms were transferred onto FluoroDish Cell Culture Dishes (World Precision Instruments). Intrinsic nanowires or Si discs were either added into culture medium or drop casted onto the biofilm and then cocultured overnight. The cocultured bacteria (with Si materials) were stained with 2 μM asante potassium green-2 AM (TEFLabs) for 1 hour at 37°C and then imaged using the Leica SP5 confocal microscope. For intrinsic nanowire stimulation experiments, a laser pulse (592 nm, 1 ms, ~79.5 mW) was delivered to the nanowire/biofilm interface of interest.

Membrane potential imaging

B. subtilis biofilms were transfer onto FluoroDish Cell Culture Dishes (World Precision Instruments). Intrinsic nanowires or Si discs were drop casted onto the biofilm and then cocultured overnight. The cocultured bacteria (with Si materials) were stained with 10 μM thioflavin T for 1 hour at 37°C and then imaged using the Leica SP5 confocal microscope. For intrinsic nanowire stimulation experiments, a laser pulse (592 nm, 1 ms,) was delivered to nanowire/biofilm interface of interest.

LIVE/DEAD assay

The cocultured bacteria (with intrinsic nanowire) were stained by the LIVE/DEAD BacLight Bacterial Viability Kit (Molecular Probes) following the manufacturer's instruction. The stained samples were imaged using the Leica SP5 confocal microscope. For all the intrinsic nanowire stimulation experiments, a laser pulse (592 nm, 1 ms) was delivered to the spots of interest. Live cells will stay green throughout the entire sequence, while dead cells will be stained red.

Microfluidic device fabrication

Microfluidic devices were prepared according to standard soft lithography and replica molding process (*43*). In brief, a thin layer of SU-8 (~5 μm) was spin coated onto an Si wafer, and specific patterns were prepared with standard photolithography procedures. Then, the prepolymer of polydimethylsiloxane (PDMS) (SYLGARD 184 from Dow Corning) was poured onto the Si wafer substrate, followed by curing in a 60°C oven for 2 hours. The PDMS mold was gently peeled off from the Si wafer, and a biopunch was used to prepare the inlets/outlets of the PDMS mold. After oxygen plasma treatment, the PDMS mold was bonded to a glass substrate, and the microfluidic devices were ready for applications.

Biofilm extracellular matrix staining

The biofilm matrix was stained by SYPRO Ruby biofilm matrix stain (Thermo Fisher Scientific). Briefly, 200 μl of the staining solution was added onto the biofilm sample, and the sample was incubated for 30 min at room temperature, protected from light. The stained biofilm samples were immersed in resin with water and then imaged using a Leica SP5 confocal microscope.

Nanoindentation

The cocultured biofilms (with Si nanowires) were stimulated using a Leica SP5 confocal microscope, and for all stimulation experiments, a laser (592 nm) was used to scan a region of interests (300× 300 μm^2) on the biofilm. (The power of the stimulation laser was estimated to be 103.1 mW.) Nanoindentation was performed on a BioSoft Indenter (Bruker Hysitron, MN) with a spherical sapphire probe ($r = 200$ μm). All of the measurements were kept at a constant loading and unloading rate of 20 μN/s to fix the impact from any potential time-dependent properties of the materials (e.g., viscoelasticity and poroelasticity) on the measurements. To extract the Young's modulus E_s of the samples, we fit the force (F)-indentation (δ) data from the loading process by a modified Hertzian contact model of a rigid sphere indenting into an elastic half space provided that the Young's modulus of the indentation probe $E_p \gg E_s$ (Eq. 1 below) (*44*)

$$F = \frac{4 E_s r^{1/2} \delta^{3/2}}{3(1 - \nu_s^2)} \quad (1)$$

Here, we assume the Poisson's ratio of the samples is $\nu_s = 0.5$, which has been widely used for biological (*45*) and soft materials (*46*). To ensure the appropriateness of the Hertzian contact model as required that $\delta \ll r$ (*44*), we only fit the data within 20-μm indentation depth (R^2 in the range of 0.9 to 0.99).

Mechanical property measurement

Various *B. subtilis* biofilms were prepared to test the mechanical properties. More specifically, nuclepore membranes (diameter, 25 mm; pore size, 0.2 μm; Whatman) were placed on top of MSgg minimal medium agar plate containing various calcium concentrations (0, 7, 700, and 7000 μM), and 2.5 μl of *B. subtilis* cell suspension (precultured in LB overnight) was dropped onto the membranes, followed by incubation at 30°C for 2 days. Rheological properties of the prepared biofilms (with membrane) were measured using TA Instruments ARES-G2 equipped with an Advanced Peltier System (APS) for temperature control. All measurements were performed using an APS flat plate for the bottom geometry and a 25-mm diameter for the upper parallel plate geometry with a nominal gap of 100 μm. A solvent trap was used to prevent water evaporation and sample drying during the measurements. During the rheology test, a small compressive force of 0.1 N was applied, and the stress growth tests were performed at a constant frequency of 5×10^{-5} rad/s. As comparisons, alginate gels that were ionically cross-linked by Ca^{2+} were prepared by the addition of 1 ml of 0, 7, 700, and 7000 μM calcium solutions, respectively, to petri dishes (35 mm) that contained sodium alginate films (2 weight % in DI water). The cross-linked gels were peeled off from the dishes for rheology tests.

Biofilm disruption experiment

The biofilms integrated with Si discs were stimulated directly with maximum power (the power-induced discs kick away from the biofilm) or gradually increased laser power to maximum power. Images were conducted by using a Leica SP5 confocal microscope. The biofilms integrated with the Si meshes were stimulated with a Leica SP5 confocal microscope. A pulse (592 nm, 1 ms, 182.0 mW) was delivered to the mesh and repeated multiple times.

Calcium signaling cellular automaton simulation

N uniformly randomly distributed sites in an l by l lattice ($N < l^2$) were chosen to represent bacteria. If the Euclidian distance between two bacteria is less than cutoff r, then they are considered neighbors. Each bacterium can adopt four states: resting, transiently activated, permanently activated, or refractory. To simulate stimulation by a circular disc of Si, all bacteria in a ring (i.e., at a distance greater than a and less than b from the center of the simulation box) were initialized in the permanently activated state. To simulate stimulation by an Si nanowire, all bacteria within distance c of the center of the simulation box are initialized in the permanently activated state. Bacteria within distance r of the boundary of the simulation box are initialized in the refractory state to create an "absorbing" boundary condition. All other bacteria are initialized in the resting state. On each discrete time step, each bacterium in the resting state that has at least one activated neighbor becomes transiently activated. On the next time step, if the proportion of a transiently activated cell's neighbors that are activated exceeds t, it becomes permanently activated. Otherwise, it becomes refractory. These state transition rules are summarized in fig. S15A. The parameters used for the simulations shown here are $N = 8000$, $l = 150$, $r = 12$, $a = 40$, $b = 43$, $c = 10$, and $t = 0.75$.

Finite element simulation

Finite element simulations were performed by using COMSOL Multiphysics to investigate the laser-induced transient heat transfer and fluid convective water flows near Si plates and nanowire structures. To simultaneously evaluate the temperature distribution and the convective water flow, the combined physics model including heat transfer in solids (discs, nanowires, and glass substrate) and fluid (water) and the fluid dynamics in laminar flow (water) was used. The buoyant force was introduced in fluid dynamics simulation to describe the

convection of water in gravity. The initial temperature for all regions was set to room temperature, and the open boundary condition was applied in both the heat transfer and fluid dynamics simulations to avoid unwanted boundary effect from the outermost boundary of the calculation domain. To simulate the laser-induced heat generation by photothermal effect, the Si discs or nanowires were placed in water at the distance of 2 μm above the glass substrate. The pulsed uniform volume heat source with the rectangular pulse shape in 1-ms period that starts from 0.2 ms was applied at the desired location in the Si discs and nanowires. The heat density defined by the laser-induced heat energy divided by the volume of heat source was used to set the amplitude of the pulsed heat source. The cross-sectional area and the thickness of the volume heat source were set to laser illumination spot size and thickness as the Si structures, respectively. The generated heat energy from the laser was obtained by calculating absorbed light energy in Si discs or nanowires from separate optical simulations. Two-dimensional axisymmetric simulation was used for the simulation with circular discs, otherwise 3D simulation was used.

SUPPLEMENTARY MATERIALS

Supplementary material for this article is available at http://advances.sciencemag.org/cgi/content/full/6/7/eaay2760/DC1

Table S1. Comparison between different intercellular communication modes in bacterial community.
Table S2. Strains and plasmids used in this study.
Fig. S1. Synthesis of *i-i* coaxial Si nanowires.
Fig. S2. TEM images of Si nanowires before and after defect-selective etching.
Fig. S3. Pseudocolored SEM images showing interactions between various bacterial cells and mesostructured nanowires.
Fig. S4. A single-layer biofilm consists of a sheet of cells embedded in the extracellular matrix.
Fig. S5. Schematic illustration of the fabrication procedures for Si microplates.
Fig. S6. Macroporous Si meshes can seamlessly integrate with biofilms.
Fig. S7. The effect of Si nanowire mesostructures on the photothermal effect and interaction with bacteria.
Fig. S8. SEM images showing that the nanowires have pretty uniform surface roughness and diameter with different etching conditions.
Fig. S9. Effects of specific heat, thermal conductivity, and light absorption on the nanowire photothermal response.
Fig. S10. Nanowire attracted bacteria right after light illumination, and the binding interface can be stable for more than 10 min.
Fig. S11. Bacteria can relocate on the same Si nanowire after sweeping the laser spot.
Fig. S12. LIVE/DEAD assays show the bacterial viability after laser illumination of single Si nanowires.
Fig. S13. Laser power determines the number of cells being attracted to the Si nanowires, regardless of the bacterial species.
Fig. S14. Nanoparticles can be attracted to the Si nanowires, regardless of the surface charges.
Fig. S15. Finite element simulation of laser-induced transient thermal distribution and corresponding fluidic convective flows.
Fig. S16. Attracted bacterial cells experienced intracellular Ca^{2+} elevation right after light illumination.
Fig. S17. Si nanowire can induce a rapid calcium wave in the biofilm.
Fig. S18. Cellular automaton model of Ca^{2+} wave propagation.
Fig. S19. Si nanowire is critical to uncover the rapid calcium signaling in *B. subtilis* biofilm.
Fig. S20. Endogenous calcium-sensitive protein further confirms the calcium signaling within *B. subtilis* biofilms.
Fig. S21. Calcium propagation under different inhibitors.
Fig. S22. Si nanowires can activate calcium signaling in *P. aeruginosa* biofilms.
Fig. S23. Intercellular calcium communications can occur across microbial species.
Fig. S24. Simulation of the size-dependent temperature distributions from Si discs with different diameters.
Fig. S25. The photothermal effect of the Si disc is inversely related to the disc size.
Fig. S26. The final calcium distribution patterns are correlated to the spatial temperature gradients right after the laser stimulation.
Fig. S27. The final calcium distribution pattern can be stable for at least 5 min.
Fig. S28. LIVE/DEAD assays show the bacterial viabilities after laser illuminations on Si discs.
Fig. S29. The spatial temperature gradient is always peaked near the disc edge rather than the center.
Fig. S30. Experimental and simulation results from Si microplates with different geometries further confirm the correlation between calcium distribution pattern and spatial gradient of temperature.
Fig. S31. Calcium signaling in conjunction with convective flows can cause biofilm disruption.
Fig. S32. Sequentially increased laser stimulations, compared with directly applying high-power laser stimulation, are more efficient to mechanically break the biofilm.
Fig. S33. Nanoindentation shows that the laser stimulation could alter the biofilm modulus.
Fig. S34. Biofilms exhibit calcium-dependent mechanical properties, similar to alginate hydrogels that are ionically cross-linked by Ca^{2+}.
Fig. S35. Ca^{2+} distributions in a living biofilm can be controlled by custom-design Si patterns.
Fig. S36. Microfluidic system for cell attraction and single-layer biofilm stimulation experiments.
Fig. S37. Si nanowire can activate potassium, calcium, and membrane signaling in *B. subtilis* biofilms.
Movie S1. Si nanowire can induce a rapid Ca^{2+} wave in *B. subtilis* biofilm.
Movie S2. Si nanowire induced Ca^{2+} signaling under inhibitor.
Movie S3. Large Si microdisc induced a bidirectional circular Ca^{2+} wave in *B. subtilis* biofilm.
Movie S4. Calcium signaling in conjunction with convective flows can cause biofilm disruption.

REFERENCES AND NOTES

1. K. Papenfort, B. L. Bassler, Quorum sensing signal–response systems in Gram-negative bacteria. *Nat. Rev. Microbiol.* **14**, 576–588 (2016).
2. A. Prindle, J. Liu, M. Asally, S. Ly, J. Garcia-Ojalvo, G. M. Süel, Ion channels enable electrical communication in bacterial communities. *Nature* **527**, 59–63 (2015).
3. S. Mukherjee, B. L. Bassler, Bacterial quorum sensing in complex and dynamically changing environments. *Nat. Rev. Microbiol.* **17**, 371–382 (2019).
4. J. Liu, A. Prindle, J. Humphries, M. Gabalda-Sagarra, M. Asally, D.-y. D. Lee, S. Ly, J. Garcia-Ojalvo, G. M. Süel, Metabolic co-dependence gives rise to collective oscillations within biofilms. *Nature* **523**, 550–554 (2015).
5. E. de Nadal, G. Ammerer, F. Posas, Controlling gene expression in response to stress. *Nat. Rev. Genet.* **12**, 833–845 (2011).
6. W. Gerstner, W. M. Kistler, *Spiking Neuron Models: Single Neurons, Populations, Plasticity* (Cambridge Univ. Press, 2002).
7. K. Richter, M. Haslbeck, J. Buchner, The heat shock response: Life on the verge of death. *Mol. Cell* **40**, 253–266 (2010).
8. I. R. Booth, M. D. Edwards, S. Black, U. Schumann, S. Miller, Mechanosensitive channels in bacteria: Signs of closure? *Nat. Rev. Microbiol.* **5**, 431–440 (2007).
9. N. M. Vega, K. R. Allison, A. S. Khalil, J. J. Collins, Signaling-mediated bacterial persister formation. *Nat. Chem. Biol.* **8**, 431–433 (2012).
10. K. K. Sakimoto, A. B. Wong, P. Yang, Self-photosensitization of nonphotosynthetic bacteria for solar-to-chemical production. *Science* **351**, 74–77 (2016).
11. J. Guo, M. Suástegui, K. K. Sakimoto, V. M. Moody, G. Xiao, D. G. Nocera, N. S. Joshi, Light-driven fine chemical production in yeast biohybrids. *Science* **362**, 813–816 (2018).
12. H. Zhang, Y. Liu, X. Nie, L. Liu, Q. Hua, G.-P. Zhao, C. Yang, The cyanobacterial ornithine–ammonia cycle involves an arginine dihydrolase. *Nat. Chem. Biol.* **14**, 575–581 (2018).
13. D. I. Piraner, M. H. Abedi, B. A. Moser, A. Lee-Gosselin, M. G. Shapiro, Tunable thermal bioswitches for in vivo control of microbial therapeutics. *Nat. Chem. Biol.* **13**, 75–80 (2017).
14. E. K. Chu, O. Kilic, H. Cho, A. Groisman, A. Levchenko, Self-induced mechanical stress can trigger biofilm formation in uropathogenic *Escherichia coli*. *Nat. Commun.* **9**, 4087 (2018).
15. J. A. Frank, J. Broichhagen, D. A. Yushchenko, D. Trauner, C. Schultz, D. J. Hodson, Optical tools for understanding the complexity of β-cell signalling and insulin release. *Nat. Rev. Endocrinol.* **14**, 721–737 (2018).
16. X. Han, X. Qian, J. G. Bernstein, H. H. Zhou, G. T. Franzesi, P. Stern, R. T. Bronson, A. M. Graybiel, R. Desimone, E. S. Boyden, Millisecond-timescale optical control of neural dynamics in the nonhuman primate brain. *Neuron* **62**, 191–198 (2009).
17. Y. Jiang, J. L. Carvalho-de-Souza, R. C. S. Wong, Z. Luo, D. Isheim, X. Zuo, A. W. Nicholls, I. W. Jung, J. Yue, D.-J. Liu, Y. Wang, V. De Andrade, X. Xiao, L. Navrazhnykh, D. E. Weiss, X. Wu, D. N. Seidman, F. Bezanilla, B. Tian, Heterogeneous silicon mesostructures for lipid-supported bioelectric interfaces. *Nat. Mater.* **15**, 1023–1030 (2016).
18. Y. Jiang, R. Parameswaran, X. Li, J. L. Carvalho-de-Souza, X. Gao, L. Meng, F. Bezanilla, G. M. G. Shepherd, B. Tian, Nongenetic optical neuromodulation with silicon-based materials. *Nat. Protoc.* **14**, 1339–1376 (2019).
19. B. Tian, T. Cohen-Karni, Q. Qing, X. Duan, P. Xie, C. M. Lieber, Three-dimensional, flexible nanoscale field-effect transistors as localized bioprobes. *Science* **329**, 830–834 (2010).
20. D.-H. Kim, N. Lu, R. Ma, Y.-S. Kim, R.-H. Kim, S. Wang, J. Wu, S. M. Won, H. Tao, A. Islam, K. J. Yu, T.-i. Kim, R. Chowdhury, M. Ying, L. Xu, M. Li, H.-J. Chung, H. Keum, M. McCormick, P. Liu, Y.-W. Zhang, F. G. Omenetto, Y. Huang, T. Coleman, J. A. Rogers, Epidermal electronics. *Science* **333**, 838–843 (2011).

21. C. Chiappini, E. De Rosa, J. O. Martinez, X. Liu, J. Steele, M. M. Stevens, E. Tasciotti, Biodegradable silicon nanoneedles delivering nucleic acids intracellularly induce localized in vivo neovascularization. *Nat. Mater.* **14**, 532–539 (2015).
22. Y. W. Jiang, X. Li, B. Liu, J. Yi, Y. Fang, F. Shi, X. Gao, E. Sudzilovsky, R. Parameswaran, K. Koehler, V. Nair, J. Yue, K. Guo, Y. Fang, H. M. Tsai, G. Freyermuth, R. C. S. Wong, C. M. Kao, C. T. Chen, A. W. Nicholls, X. Wu, G. M. G. Shepherd, B. Tian, Rational design of silicon structures for optically controlled multiscale biointerfaces. *Nat. Biomed. Eng.* **2**, 508–521 (2018).
23. Z. Luo, Y. Jiang, B. D. Myers, D. Isheim, J. Wu, J. F. Zimmerman, Z. Wang, Q. Li, Y. Wang, X. Chen, V. P. Dravid, D. N. Seidman, B. Tian, Atomic gold–enabled three-dimensional lithography for silicon mesostructures. *Science* **348**, 1451–1455 (2015).
24. R. Gómez-Martínez, A. M. Hernández-Pinto, M. Duch, P. Vázquez, K. Zinoviev, E. J. de la Rosa, J. Esteve, T. Suárez, J. A. Plaza, Silicon chips detect intracellular pressure changes in living cells. *Nat. Nanotechnol.* **8**, 517–521 (2013).
25. H. Fang, K. J. Yu, C. Gloschat, Z. Yang, E. Song, C.-H. Chiang, J. Zhao, S. M. Won, S. Xu, M. Trumpis, Y. Zhong, S. W. Han, Y. Xue, D. Xu, S. W. Choi, G. Cauwenberghs, M. Kay, Y. Huang, J. Viventi, I. R. Efimov, J. A. Rogers, Capacitively coupled arrays of multiplexed flexible silicon transistors for long-term cardiac electrophysiology. *Nat. Biomed. Eng.* **1**, 0038 (2017).
26. J.-H. Park, L. Gu, G. von Maltzahn, E. Ruoslahti, S. N. Bhatia, M. J. Sailor, Biodegradable luminescent porous silicon nanoparticles for in vivo applications. *Nat. Mater.* **8**, 331–336 (2009).
27. H.-C. Flemming, J. Wingender, U. Szewzyk, P. Steinberg, S. A. Rice, S. Kjelleberg, Biofilms: An emergent form of bacterial life. *Nat. Rev. Microbiol.* **14**, 563–575 (2016).
28. B. Tian, X. Zheng, T. J. Kempa, Y. Fang, N. Yu, G. Yu, J. Huang, C. M. Lieber, Coaxial silicon nanowires as solar cells and nanoelectronic power sources. *Nature* **449**, 885–889 (2007).
29. F. Secco d'Aragona, Dislocation etch for (100) planes in silicon. *J. Electrochem. Soc.* **119**, 948–951 (1972).
30. P. B. Roder, B. E. Smith, E. J. Davis, P. J. Pauzauskie, Photothermal heating of nanowires. *J. Phys. Chem. C* **118**, 1407–1416 (2014).
31. L. Lin, X. Peng, Z. Mao, W. Li, M. N. Yogeesh, B. B. Rajeeva, E. P. Perillo, A. K. Dunn, D. Akinwande, Y. Zheng, Bubble-pen lithography. *Nano Lett.* **16**, 701–708 (2015).
32. C. Zhao, Y. Xie, Z. Mao, Y. Zhao, J. Rufo, S. Yang, F. Guo, J. D. Mai, T. J. Huang, Theory and experiment on particle trapping and manipulation via optothermally generated bubbles. *Lab Chip* **14**, 384–391 (2014).
33. Y. Zheng, H. Liu, Y. Wang, C. Zhu, S. Wang, J. Cao, S. Zhu, Accumulating microparticles and direct-writing micropatterns using a continuous-wave laser-induced vapor bubble. *Lab Chip* **11**, 3816–3820 (2011).
34. J. Chen, H. Cong, F.-C. Loo, Z. Kang, M. Tang, H. Zhang, S.-Y. Wu, S.-K. Kong, H.-P. Ho, Thermal gradient induced tweezers for the manipulation of particles and cells. *Sci. Rep.* **6**, 35814 (2016).
35. D. E. Clapham, Calcium signaling. *Cell* **131**, 1047–1058 (2007).
36. M. Toyota, D. Spencer, S. Sawai-Toyota, W. Jiaqi, T. Zhang, A. J. Koo, G. A. Howe, S. Gilroy, Glutamate triggers long-distance, calcium-based plant defense signaling. *Science* **361**, 1112–1115 (2018).
37. L. Leybaert, M. J. Sanderson, Intercellular Ca^{2+} waves: Mechanisms and function. *Physiol. Rev.* **92**, 1359–1392 (2012).
38. R. Thar, M. Kühl, Bacteria are not too small for spatial sensing of chemical gradients: An experimental evidence. *Proc. Natl. Acad. Sci. U.S.A.* **100**, 5748–5753 (2003).
39. H.-C. Flemming, J. Wingender, The biofilm matrix. *Nat. Rev. Microbiol.* **8**, 623–633 (2010).
40. S. Inouye, M. Noguchi, Y. Sakaki, Y. Takagi, T. Miyata, S. Iwanaga, T. Miyata, F. I. Tsuji, Cloning and sequence analysis of cDNA for the luminescent protein aequorin. *Proc. Natl. Acad. Sci. U.S.A.* **82**, 3154–3158 (1985).
41. H. Jarmer, R. Berka, S. Knudsen, H. H. Saxild, Transcriptome analysis documents induced competence of Bacillus subtilis during nitrogen limiting conditions. *FEMS Microbiol. Lett.* **206**, 197–200 (2002).
42. I. Torrecilla, F. Leganés, I. Bonilla, F. Fernández-Piñas, Use of recombinant aequorin to study calcium homeostasis and monitor calcium transients in response to heat and cold shock in cyanobacteria. *Plant Physiol.* **123**, 161–176 (2000).
43. Y. Xia, G. M. Whitesides, Soft lithography. *Angew. Chem. Int. Ed.* **37**, 550–575 (1998).
44. J. W. Harding, I. N. Sneddon, The elastic stresses produced by the indentation of the plane surface of a semi-infinite elastic solid by a rigid punch. *Math. Proc. Cambridge Philos. Soc.* **41**, 16–26 (2008).
45. A. Samani, J. Zubovits, D. Plewes, Elastic moduli of normal and pathological human breast tissues: An inversion-technique-based investigation of 169 samples. *Phys. Med. Biol.* **52**, 1565–1576 (2007).
46. K. S. Anseth, C. N. Bowman, L. Brannon-Peppas, Mechanical properties of hydrogels and their experimental determination. *Biomaterials* **17**, 1647–1657 (1996).

Acknowledgments: We would like to thank R. Haselkorn for the useful discussion during this project and O. Zaborina for providing *P. aeruginosa*. We thank K. Watters for scientific editing of the manuscript. This work made use of instruments in the Electron Microscopy Service (Research Resources Center, UIC). **Funding:** B.T. acknowledges support from Office of Naval Research (ONR YIP, N000141612530; PECASE, N000141612958). H.-G.P. acknowledges support from the National Research Foundation of Korea (NRF) grant funded by the Korean government (MSIT) (2018R1A3A3000666). A.R.D. acknowledges support from the Materials Research Science and Engineering Centers (MRSEC) and National Science Foundation (NSF) Division of Material Science (DMR)-1420709. K.-H.K. acknowledges support from the National Research Foundation of Korea (NRF) grant funded by the Korean government (MSIT) (2019R1C1C1006681). **Author contributions:** X.G., Y.J., Y.L., and B.T. designed the research. K.-H.K., H.-C.L., and H.-G.P. designed and performed finite element simulations. Z.L., O.L., R.Z., and A.R.D. performed calcium signaling simulation. X.G. performed the bacteria experiments. Y.J., X.G., Y.F., J.Y., L.M., and W.F. fabricated the materials. Y.L. performed the microfluidic experiments. Y.L., Y.J., and F.S. performed the electron microscope imaging. Q.T. performed the nanoindentation and analyzed the data with assistance from G.S.S. W.F. performed zeta potential measurements. X.G. performed the mechanical property measurement with help from Y.F., P.J.G., and Y.L. V.N. performed the fluorometer measurements. X.G., Y.J., Y.L., and B.T. wrote the paper and received comments and edits from all authors. B.T. and H.-G.P. mentored the research. **Competing interests:** The authors declare that they have no competing interests. **Data and materials availability:** All data needed to evaluate the conclusions in the paper are present in the paper and/or Supplementary Materials. Additional data related to this paper can be requested from the authors.

Submitted 4 June 2019
Accepted 26 November 2019
Published 14 February 2020
10.1126/sciadv.aay2760

Citation: X. Gao, Y. Jiang, Y. Lin, K.-H. Kim, Y. Fang, J. Yi, L. Meng, H.-C. Lee, Z. Lu, O. Leddy, R. Zhang, Q. Tu, W. Feng, V. Nair, P. J. Griffin, F. Shi, G. S. Shekhawat, A. R. Dinner, H.-G. Park, B. Tian, Structured silicon for revealing transient and integrated signal transductions in microbial systems. *Sci. Adv.* **6**, eaay2760 (2020).